INTERACTION OF MICROPHYSICAL AND DYNAMICAL TIMESCALES IN OROGRAPHIC PRECIPITATION

A. Muhlbauer*, P. Spichtinger and U. Lohmann
Institute for Atmospheric and Climate Science, ETH Zurich, Switzerland

1. INTRODUCTION

The development of orographic precipitation depends on the interaction of processes which operate on different timescales (Smith 1979; Jiang and Smith 2003; Smith and Barstad 2004; Kirshbaum and Durran 2004; Roe and Baker 2006). Dynamical timescales are inherent to the flow dynamics (e.g. advection timescale, timescale of instability growth) and can be distinguished from timescales governed by microphysical processes (e.g hydrometeor conversion timescale, timescale of hydrometer fallout). The interaction between these different timescales controls the development of orographic clouds and determines the orographic precipitation distribution. So far, the relevance of dynamical and microphysical timescales for orographic precipitation has only been analyzed within the framework of linear models (Smith 1979; Smith and Barstad 2004) or with numerical models and simplified microphysics (Jiang and Smith 2003; Kirshbaum and Durran 2004). Recent studies indicate that the interaction of these timescales may also be relevant for aerosol-cloud-precipitation interactions in orographic clouds (Muhlbauer and Lohmann 2008). Here, aerosol particles act as cloud condensation nuclei (CCN) and influence microphysical properties of clouds by shifting the cloud droplet size spectrum towards smaller radii. Due to the smaller collision efficiencies of the smaller cloud droplets the development of precipitation is retarded which presumably leads to a reduction in warm-phase orographic precipitation through the aerosol indirect effect. Simulations by Muhlbauer and Lohmann (2008) indicate that in the case of orographic clouds the magnitude of the indirect aerosol effect on precipitation depends strongly on the flow dynamics and on geometrical aspects of the terrain. The question arising in this context is, if it is possible to understand the magnitude (and maybe also the sign) of aerosol effects on orographic precipitation qualitatively by considering the interaction of the timescales most important for orographic precipitation (e.g. timescale of advection, microphysical timescales).

The main goal of this study is to identify the important and dominant timescales for the orographic precipitation development in a state-of-the-art numerical model and to quantify their role in different dynamical and thermodynamical regimes. A further goal of this work is to investigate the effect of aerosols on the microphysical timescales and the feedbacks on the orographic precipitation distribution in warm-phase orographic clouds.

* *Corresponding author address:* Andreas Muhlbauer, Institute for Atmospheric and Climate Science, ETH Zurich, Universitaetsstrasse 16, 8092 Zurich, Switzerland.
E-mail: andreas.muehlbauer@env.ethz.ch

The paper is structured as follows: In section 2 we briefly introduce the modeling approach focusing on the numerical model and the parameterizations which are employed. In section 3 we discuss the model setup, the initial conditions and the experimental design. In section 4 we present the model simulation and discuss our results in section 5.

2. NUMERICAL MODEL

The model simulations are performed with the nonhydrostatic, fully compressible limited-area mesoscale weather prediction model COSMO[1] (Doms and Schättler 2002; Steppeler et al. 2003). The elastic equations are solved in a split-explicit time-splitting approach (Wicker and Skamarock 2002) with a two time-level total variation diminishing (TVD) 3rd order Runge-Kutta scheme in combination with a 5th order horizontal advection scheme. All prognostic moisture and aerosol variables are advected by a 2nd order positive-definite advection scheme after Bott (1989).

Since the main focus of this study is given to aerosol-cloud-precipitation interactions via the aerosol indirect effect all radiative effects such as the change in cloud albedo are neglected. Thus, no radiation parameterization is considered here.

For the vertically turbulent diffusive processes, a 2.5 level Mellor-Yamada scheme with a prognostic TKE (turbulent kinetic energy) equation is used (Herzog et al. 2002).

The coupled cloud-microphysical and aerosol-microphysical processes are treated in a two-moment bulk approach. The aerosol-microphysical processes which are considered in the model are the nucleation of gas-phase sulfuric acid, the condensation of sulfuric acid on pre-existing aerosol particles, coating of insoluble aerosols by sulfuric acid, inter- and intramodal coagulation and the uptake of water vapor. The cloud-microphysics parameterization accounts for the activation of aerosols to cloud droplets, condensation/evaporation of cloud droplets, autoconversion of cloud droplets to rain, accretion of cloud droplets by rain, self-collection of cloud droplets by rain, evaporation of rain and the break-up of large rain drops. For a more in detail explanation of the processes and the underlying model equations we refer to Seifert and Beheng (2006) and Muhlbauer and Lohmann (2008).

[1] COnsortium for Small-scale MOdeling, http://www.cosmo-model.org

3. MODEL SETUP

3a. *COMPUTATIONAL DOMAIN*

The 3D computational domain is composed of 200 times 100 gridpoints in the horizontal with a grid spacing of 2 km which yields a domain of -200 km $\leq$ x $\leq$ 200 km along the x-axis and -100 km $\leq$ y $\leq$ 100 km along the y-axis. At the lateral model boundaries an open relaxation boundary condition (Davies 1976) is introduced in the x-direction whereas periodic boundaries are prescribed in the y-direction. At the model bottom a free-slip boundary condition is used. A Rayleigh damping sponge layer is introduced at the upper rigid boundary to damp reflections of vertically propagating gravity waves. The damping layer starts at 10 km height and covers approximately one half of the vertical model domain. A terrain following SLEVE coordinate system (Schär et al. 2002) is introduced in the vertical with 60 layers and a vertical grid spacing varying between 10 m in the lowermost and approximately 1400 m in the uppermost layer. The model top is located at roughly 23 km height and the timestep of the model is 10 s.

3b. *IDEALIZED TOPOGRAPHY*

The idealized topography has the form of a 3D finite mountain ridge (Kirshbaum and Durran 2005) such that

$$h(x,y) = \begin{cases} \frac{h_0}{16}\left[1+\cos(\pi r)\right]^4 & , \; r \leq 1 \\ 0 & , \; r > 1 \, , \end{cases} \tag{1}$$

and

$$r^2 = \begin{cases} \left(\frac{x-x_0}{4a}\right)^2 + \left(\frac{|y-y_0|-B}{4b}\right)^2 & , \; |y-y_0| > B \\ \left(\frac{x-x_0}{4a}\right)^2 & , \; |y-y_0| \leq B \end{cases} \tag{2}$$

Here, h_0 is the peak height of the mountain ridge, a is the mountain half-width in x-direction, b is the mountain half-width in y-direction and the parameter B controls the width of the mountain ridge line. The mountain range is centered in the computational domain at $x_0 = 100$ and $y_0 = 50$ in gridpoint space. Unless otherwise stated we use the idealized topography with the parameters $h_0 = 1000$ m, $a = 20$ km, $b = 10$ km and $B = 30$ km.

3c. *DYNAMICAL INITIAL CONDITION*

The model is initialized with a horizontally homogeneous basic state which is given by a dry atmosphere at rest with surface pressure $\bar{p}_{SL}$ and surface temperature $\bar{T}_{SL}$. The basic state is hydrostatically balanced and the temperature increases with the logarithm of pressure such that $\partial \bar{T} / \partial \ln \bar{p} = 42$ K. The initial horizontally homogeneous profiles of pressure $p(z)$ and temperature $T(z)$ are calculated analytically as a function of surface pressure p_{SL}, surface temperature T_{SL} and the dry Brunt-Väisälä frequency N_d by following Clark and Farley (1984).

The model basic state is made similar to the actual state by setting $\bar{p}_{SL} = p_{SL}$ and $\bar{T}_{SL} = T_{SL}$ so that

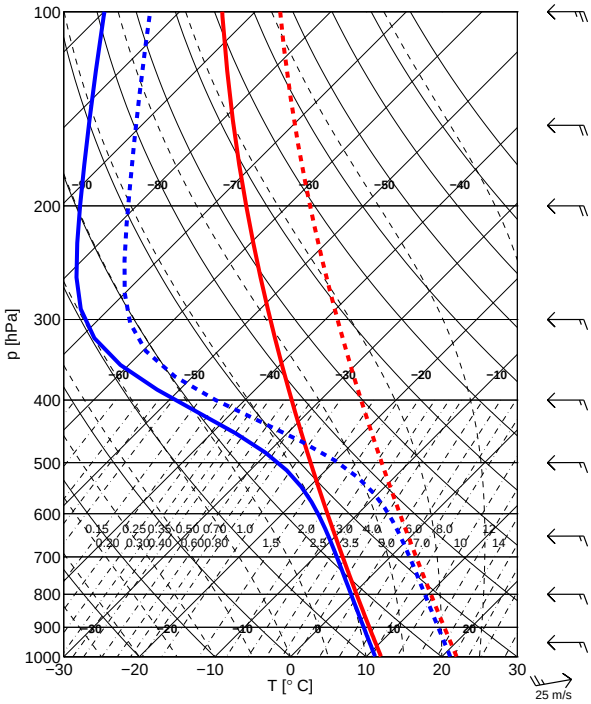

Figure 1: Atmospheric soundings for the idealized simulations showing the temperature (red) and dewpoint temperature (blue) in a skewT-logp diagram. The soundings are given analytically with the surface temperatures $T_{sl} = 285$ K (solid) and $T_{sl} = 295$ K (dashed). The dry Brunt-Väisälä frequency is $N_d = 0.011$ s^{-1} and the surface pressure is $p_{sl} = 1000$ hPa. The windspeed is $U = 15$ m s^{-1} and is prescribed constant with height within the first 10 km and increases linearly above.

the difference between the two states arises solely from the vertical temperature gradient. In our simulations, the surface pressure is $p_{SL} = 1000$ hPa and the surface temperature is prescribed by the set of temperatures $T_{SL} = 285$ K and $T_{SL} = 295$ K, re-

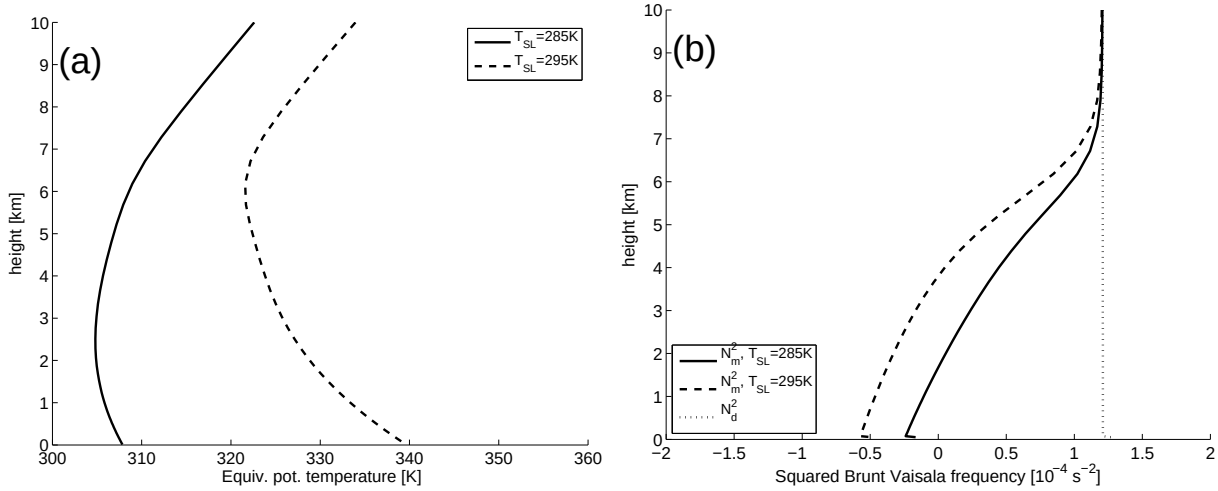

Figure 2: Vertical profiles of equivalent potential temperature (a) and squared Brunt Väisäla frequency (b) for the sounding with $T_{SL} = 285$ K (solid) and $T_{SL} = 295$ K (dashed), respectively. The dry squared Brunt-Väisäla frequency (dotted) is shown for comparison.

spectively. The dry Brunt-Väisälä frequency is chosen to be constant with height with $N_d = 0.011$ s^{-1}. The vertical profile of the relative humidity is prescribed by a modified Fermi function (Spichtinger 2004) of the type

$$RH(z) = a + \frac{b-a}{1+\exp\left[-c\,(z-z_0)\right]} \qquad (3)$$

with the parameters $a = 0.95$, $b = 0.03$, $c = 0.0015$ m^{-1}, $z_0 = 6000$ m and $0 \leq RH \leq 1$. The vertical decay of the relative humidity profile is controlled with the parameters c and z_0. The modified Fermi function gives a vertical profile of relative humidity which starts with the value $RH = 0.95$ at the surface and decays smoothly with height towards the value $RH = 0.03$. Figure 1 shows the resulting vertical profiles of temperature and dewpoint temperature in a skew T-log P chart. The horizontal wind profile U is prescribed unidirectionally and the windspeed is vertically constant with $U = 15$ m s^{-1} up to 10 km and increases linearly above to 40 m s^{-1}. Both soundings are potentially and statically unstable as shown by the vertical profiles of the equivalent potential temperature θ_e and the squared Brunt-Väisäla frequency N_m^2 (see figure 2). The lifting condensation level (LCL) is comparable in both soundings and is located at approximately $z_{LCL} \approx 100$ m altitude. The depth of the unstable layer varies in both soundings and is roughly 1500 m in the cold sounding ($T_{SL} = 285$ K) and approximately 3600 m in the warm sounding ($T_{SL} = 295$ K).

Thus, we may expect pre-existing thermal perturbations to grow in the unstable environment and to initiate convective motions in the orographic cloud. To initiate convective motions in the statically unstable regions, small-amplitude perturbations are generated and are added to the temperature stratification at the lowermost model level. The small-amplitude perturbations are drawn from a Gaussian distribution with zero mean and scaled to a root-mean-

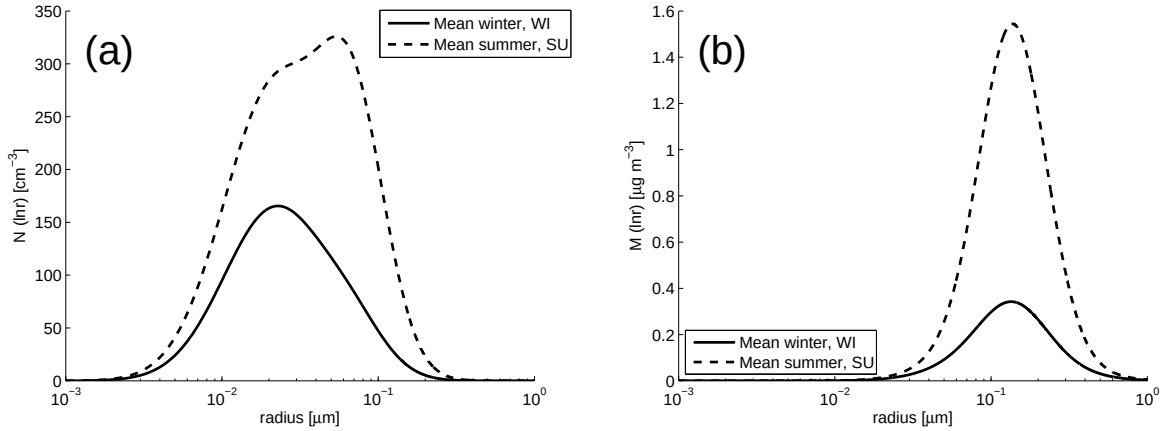

Figure 3: Aerosol initial condition for the idealized simulations. Panel (a) shows the aerosol number distribution for wintertime conditions (solid) and for summertime conditions (dashed). The aerosol spectra are seasonal means over wintertime and summertime conditions at the JFJ in Switzerland. The mass distribution is calculated analytically from the number distribution by assuming a mean density of $\rho = 1.5$ g cm^{-3} which was determined by an AMS mass closure in Cozic et al. (2007).

squared (rms) amplitude of 0.1 K (not shown). In order to remove all 2Δ structures the Gaussian perturbation field is filtered twenty times with a simple Laplacian filter operator. Since the Rossby number $Ro = U/fL$ is usually much greater than unity for the characteristic scales which are considered here ($U = 15$ m s^{-1}, $f \approx 10^{-4}$ s^{-1} at midlatitudes and $L = 20$ km), the effect of the Coriolis force is neglected in this study. Moreover, model simulations by Colle (2004) showed that the inclusion of rotation has little impact on the orographic precipitation sensitivity.

3d. *MICROPHYSICAL INITIAL CONDITION*

The initial aerosol spectra shown in figure 3 are seasonal means of wintertime (WI) and summertime (SU) aerosol size distribution measurements taken with a scanning mobility particle sizer (SMPS) at the Jungfraujoch (JFJ) in central Switzerland (Weingartner et al. 1999). The high-altitude research station at the JFJ is a free-tropospheric site during wintertime where aerosol number concentrations are generally low.

	Mode	N [cm^{-3}]	r [μm]	σ	M [μg m^{-3}]
Winter	AIT	310	0.022	2.13	0.07
	ACC	40	0.070	1.61	0.44
Summer	AIT	530	0.022	2.13	0.26
	ACC	260	0.070	1.61	1.74

Table 1: Parameters of the aerosol size distribution. The mass density M in each mode is computed from the aerosol size distribution by assuming a mean aerosol density of $\rho = 1.5$ cm^{-3} (Cozic et al. 2007). The total aerosol mass densities are $M_{WI} = 0.51$ μg m^{-3} for the winter aerosol spectrum and $M_{SU} = 2.0$ μg m^{-3} for the summer aerosol spectrum. The abbreviations AIT and ACC denote the Aitken mode and accumulation mode, respectively.

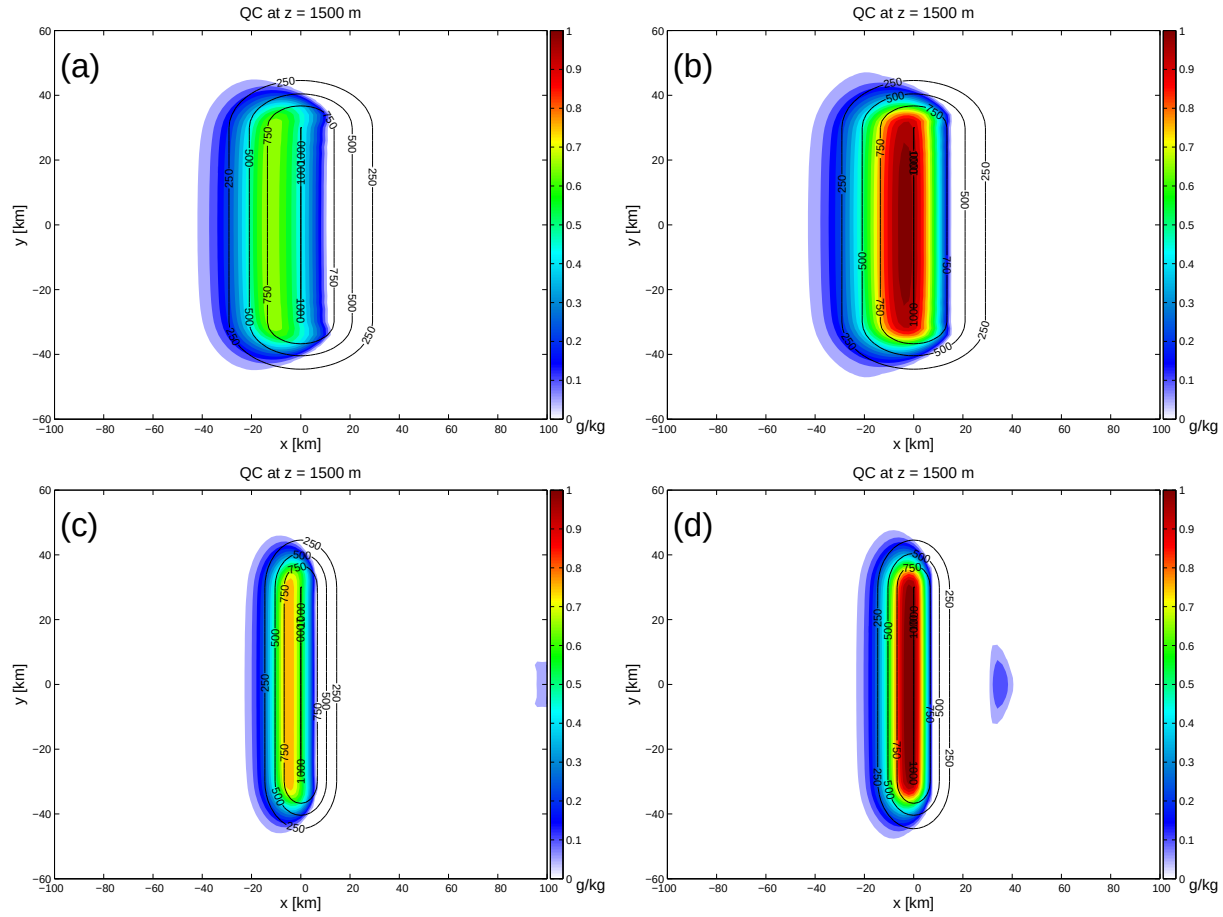

Figure 4: Cloud liquid water mixing ratio QC at $z = 1500$ m height and contours of the underlying topography. The simulation with wintertime (WI) aerosol conditions are shown in the left panels (a) and (c) whereas the simulations with the summertime (SU) aerosol conditions are shown in the right panels (b) and (d). The half-width of the finite mountain ridge is $a = 20$ km in the upper panels (a) and (b) whereas it is $a = 10$ km in the lower panels (c) and (d). Only parts of the computational domain are plotted.

During summertime the air at the JFJ is no longer decoupled from the Alpine boundary layer and convective processes as well as slope wind circulations transport boundary layer air to the JFJ which leads to a general increase in aerosol number concentrations during the summer (Weingartner et al. 1999; Choularton et al. 2008). The aerosol spectra satisfy a lognormal size distribution of the form

$$N(\ln r) = \sum_{i=1}^{2} \frac{N_i}{\sqrt{2\pi}\ln\sigma_i} \exp\left[-\left(\frac{\ln r - \ln \tilde{r}_i}{\sqrt{2}\ln\sigma_i}\right)^2\right] \tag{4}$$

with the three free parameters being the aerosol

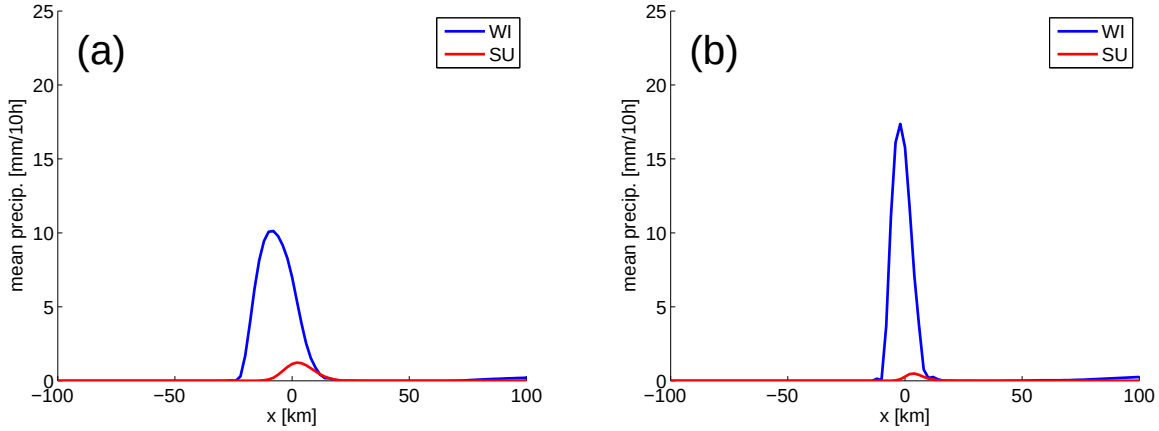

Figure 5: Precipitation distribution along the topography for the simulation with wintertime (WI) aerosol (blue) and summertime (SU) aerosol (red), respectively. The half-width of the idealized topography is $a = 20$ km in panel (a) and $a = 10$ km in panel (b).

number densities N_i, the count median radii $\tilde{r}_i$ and the geometric standard deviations σ_i. The specific parameters of the lognormal aerosol size distribution are summarized in table 1. The aerosol initial condition is prescribed vertically constant. Assuming a mean density of the aerosol of $\rho = 1.5$ g cm^{-3} the mass distribution of the aerosols can be calculated directly from the number distribution. The mean aerosol density of $\rho = 1.5$ g cm^{-3} was obtained by an aerosol mass spectrometry (AMS) mass closure in Cozic et al. (2007). Integration over the mass distributions yields the aerosol mass densities (in this case $\approx$ PM1) which are $M_{SU} = 2.0$ μg m^3 and $M_{WI} = 0.51$ μg m^3.

4. MODEL SIMULATIONS

In the following section we consider 3D simulations of moist flows past topography for the two thermodynamically distinct initial conditions ($T_{SL} = 285$ K and $T_{SL} = 295$ K) discussed in section 3. The aerosol initial conditions are initialized with the observed aersol size distributions. Since the mean summertime aerosol size spectrum exhibits considerably larger aerosol number concentrations than the mean wintertime aerosol spectrum we consider simulations with the summertime aerosol spectrum as polluted (in the following denoted with SU) and the simulations with the wintertime aerosol spectrum as clean (in the following denoted with WI). However, since the aerosol measurements were obtained at a high-altitude research station the aerosol concentrations are typical for remote-continental conditions in central Switzerland.
Since the characteristic nondimensional mountain height $\hat{h} = N_d h/U$ is approximately $\hat{h} = 0.73$ for our setup, we expect the orographic flow to develop structures of a linear hydrostatic mountain wave.

4a. *Stratiform orographic precipitation*

At first we consider the flow over a mountain range with a characteristic mountain half-width of $a =$

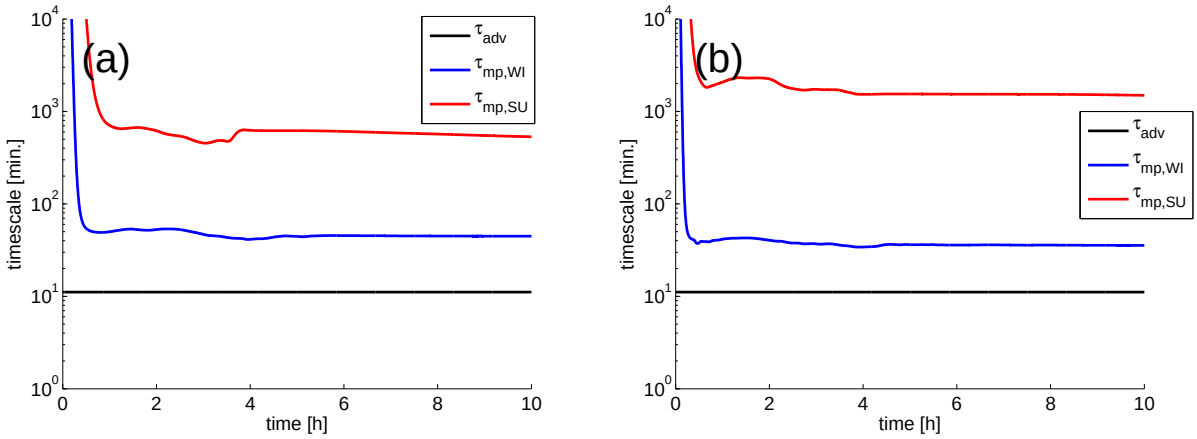

Figure 6: Dynamical and microphysical timescales. The dynamical timescale for advection τ_{adv} (black) is shown together with the microphysical timescale τ_{mp} for the simulation with wintertime aerosol spectrum (WI) and the simulation with summertime aerosol spectrum (SU). The simulation with wide mountain ($a = 20$ km) is shown in panel (a) whereas the simulation with narrow mountain ($a = 10$ km) is shown in panel (b).

20 km. The resulting field of cloud liquid water after 10 h simulation time is shown in figure 4. A stable orographic cloud forms on the upslope side of the mountain as a result of the forced upslope ascent with maximum cloud liquid water mixing ratios on the order of 0.7 g kg. The simulations SU with increased aerosol number concentrations show considerably higher values of cloud liquid water of up to 1.0 g kg. Similar results are obtained if the mountain half-width is reduced to $a = 10$ km although the lifting imposed by the mountain wave is stronger in this case. Again, cloud liquid water increases in the simulations with higher aerosol number concentrations.

Figure 5 shows the averaged precipitation distribution along the topography after 10 h of simulation. The simulation with increased aerosol number concentrations depict a clear downstream shift of the orographic precipitation regardless of the width of the mountain. However, the upslope component of the orographic precipitation is lower in the case of the narrow mountain ($a = 10$ km) than in case of the wide mountain ($a = 20$ km). The loss in orographic precipitation at the divide is as much as 90 $\%$ in the case of the wide mountain whereas the loss is almost 97 $\%$ in the case of the narrow mountain. Similar to the results by Muhlbauer and Lohmann (2008), the magnitude of the indirect aerosol effect on precipitation depends also on geometrical aspects of the mountain range. This effect can qualitatively be understood by comparing the timescales of advection as well as the microphysical timescale to develop precipitation in both simulations as shown in figure 6.

Therefore, we approximate the advective timescale (i.e. the time it takes an airparcel to travel over the mountain) with

$$\tau_{adv} = a/U \tag{5}$$

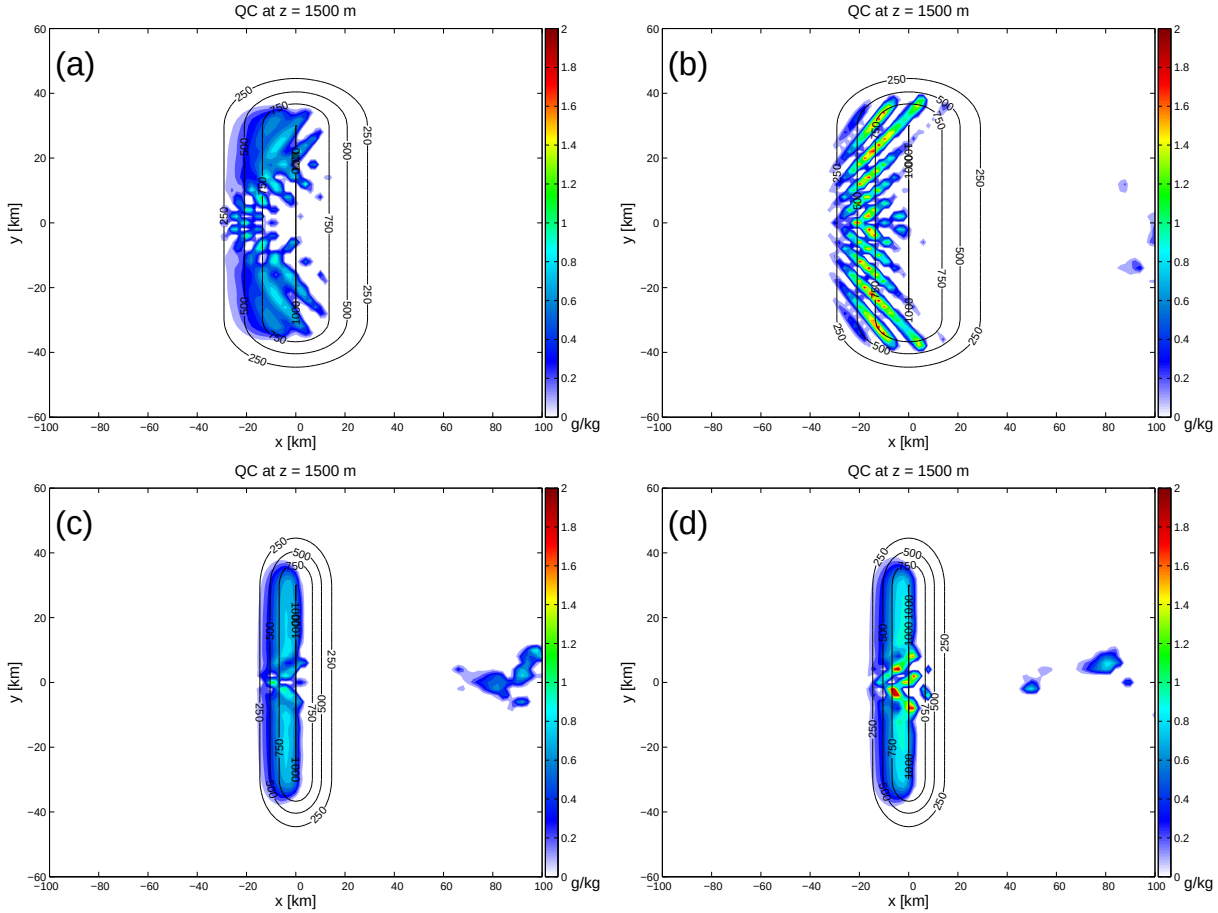

Figure 7: Same as figure 4 but for the simulations with $T_{SL} = 295$ K.

as the ratio of the mountain half-width a to the mean incoming windspeed U which yields $\tau_{adv} = 11$ min. for the narrow mountain range and $\tau_{adv} = 22$ min. for the wide mountain range. The microphysical timescales τ_{mp} (i.e. the time to convert water vapor to precipitation) is determined directly from the model simulations from the timescales of autoconversion and accretion such that

$$\tau_{mp} = \frac{L_c}{\left(\frac{\partial L_c}{\partial t}\right)_{AU} + \left(\frac{\partial L_c}{\partial t}\right)_{AC}} \tag{6}$$

with L_c the cloud liquid water content. The conversion rates for the cloud water mass are $\left(\frac{\partial L_c}{\partial t}\right)_{AU}$ for autoconversion and $\left(\frac{\partial L_c}{\partial t}\right)_{AC}$ for accretion.

For a detailed discussion on the parameterization of autoconversion and accretion we refer to Seifert and Beheng (2006). The conversion rates of e.g. condensation and nucleation are assumed to be small and, thus, are neglected. Comparing the timescales for the simulation WI and SU in figure 6 reveals that the microphysical timescale τ_{mp} is much larger in the simulation SU than in the simulation WI and also

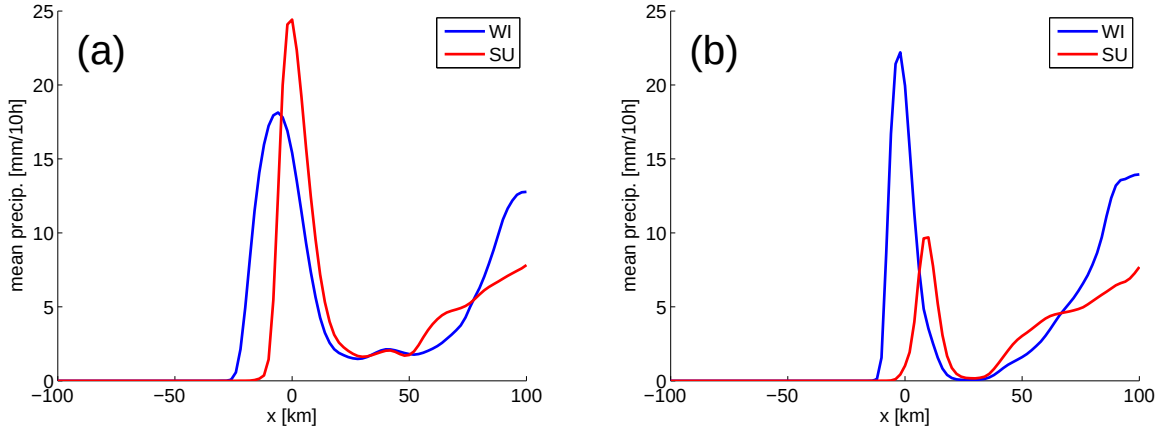

Figure 8: Same as figure 5 but for the simulations with $T_{SL} = 295$ K. The half-width of the idealized topography is $a = 20$ km in panel (a) and $a = 10$ km in panel (b).

much larger than the advective timescale. This may be interpreted such that the advection time of an air-parcel in the updraft region of the mountain wave is to short to yield a conversion of the cloud water to rain by autoconversion and accretion. Because the advection time is a function of the mountain width explains qualitatively why the aerosol indirect effect on precipitation is larger for the narrow mountain than for the wide mountain.

4b. *Convective orographic precipitation*

In the second example we repeat our simulations with the unstable sounding with $T_{SL} = 295$ K discussed in section 3. The fields of cloud liquid water are shown in figure 7 after 10 h of simulation. In contrast to the previous simulations which developed a single contiguous orographic clouds the orographic cloud breaks up into multiple small convective cells on the upslope side of the mountain embedded in the mean cross barrier flow. At the centerline the cells develop small cellular convective structures whereas at the flanks of the mountain the convective cells organize themselves into elongated rainbands. Similar to the previous simulations the cloud liquid water is increased with increasing aerosol number concentrations. Increasing the aerosol number concentrations lead also to an interesting dynamical feedback on the convective clouds which is exhibited in a higher degree of organization of the elongated rainbands.
Similar features in the cloud development are evident in the simulation with the narrow mountain. In both cases (WI and SU) reducing the mountain width does not allow the convective clouds to break up and to organize themselves into rainbands. However, small convective cells develop on the upslope side of the mountain close to the centerline which are advected to the leeward side by the cross-barrier flow and contribute to the leeward precipitation pattern. The convective cells are more strongly developed if the aerosol number concentrations are increased and exhibit higher liquid water contents. The precipitation distribution for the convective orographic precipitation case is shown in figure 8. In the case of the wide mountain ($a = 20$ km) the

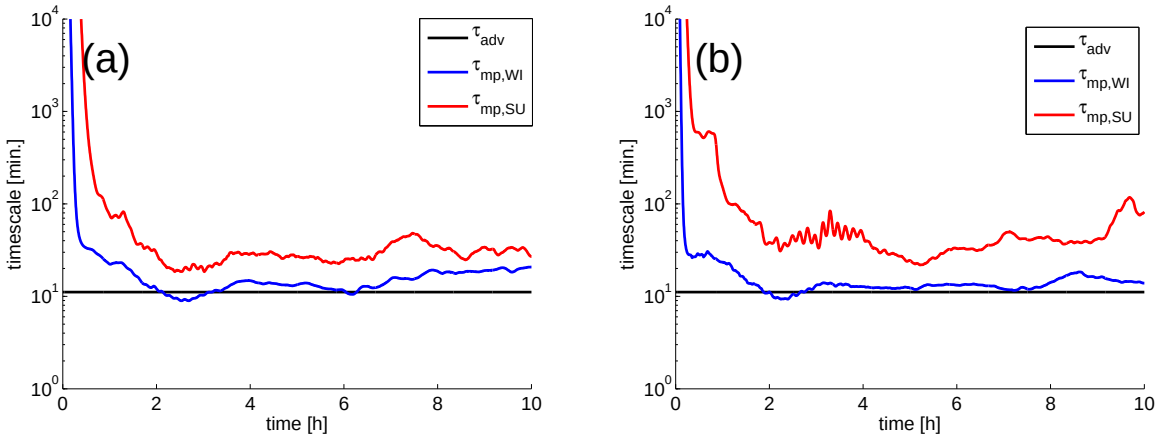

Figure 9: Same as figure 6 but for the simulations with $T_{SL} = 295$ K. The simulation with wide mountain ($a = 20$ km) is shown in panel (a) whereas the simulation with narrow mountain ($a = 10$ km) is shown in panel (b).

precipitation is reduced on the upslope side of the mountain but increased close to the mountain top and on the leeward side of the mountain. In the simulation with narrow mountain a similar orographic precipitation pattern can be found but, again, the precipitation distribution is shifted towards the leeward side of the mountain. In both simulation an increase in the aerosol number concentrations leads to a decrease in the upslope component of the orographic precipitation but also to a reduction of the total orographic precipitation. Similar to the previous simulations the overall precipitation loss is smaller in the simulation with wide mountain ($13\ \%$) than in the simulation with narrow mountain ($41\ \%$). The timescales for the convective orographic precipitation case are shown in figure 9. In the wide mountain case the microphysical timescales are on the same order of magnitude and are comparable to timescale of advection leading to a relatively small indirect aerosol effect. In contrast, the microphysical timescale is larger in the simulation with increased aerosol load and is considerably larger than the advective timescale if the mountain width is decreased which leads to a larger indirect aerosol effect on orographic precipitation for narrow mountain ranges. However, the differences between the microphysical timescales induced by the aerosol concentrations are much lower in the convective orographic precipitation case than in the stratiform suggesting that other dynamical timescales besides the advection timescale are important in this case.

5. DISCUSSION AND OUTLOOK

In this paper timescales relevant for the orographic precipitation development are analyzed in view of the indirect aerosol effect. It turns out, that for stratiform as well as convective orographic precipitation a qualitative understanding on the magnitude of the indirect effect on orographic precipitation can be established by comparing the advective timescale (i.e. the timescale of airparcels in the updraft region of a mountain wave) to the microphys-

ical timescale (i.e. the time required to transform water vapor into precipitation). However, the advection timescale alone is not able to explain why the indirect aerosol effect is much lower for convective orographic precipitation than for stratiform orographic precipitation and why the formation of elongated rainbands is enforced if the aerosol number is increased. This suggest that additional relevant timescales exist (e.g. timescale for convective growth) which are important for the development of orographic precipitation and for magnitude of the indirect aerosol effect on orographic precipitation. Investigating these timescales and their role in explaining aerosol-cloud-precipitation interactions in warm-phase and mixed-phase orographic clouds is subject to further research.

Acknowledgments

We thank Axel Seifert from the German Weather Service (DWD) and Oliver Fuhrer from the Swiss National Weather Service (MeteoSwiss). We acknowledge the European Centre for Medium-range Weather Forecasts (ECMWF) for providing computing time within the special project Cloud-Aerosol Interactions (SPCHCLAI) and the financial support provided by the International Conference on Clouds and Precipitation (ICCP).

References

Bott, A., 1989: A positive definite advection scheme obtained by nonlinear renormalization of the advective fluxes. *Mon. Weather Rev.*, **117**, 1006–1015.

Choularton, T., K. Bower, E. Weingartner, I. Crawford, H. Coe, M. Gallagher, M. Flynn, J. Crosier, P. Connolly, A. Targino, M. Alfarra, U. Baltensperger, S. Sjogren, B. Verheggen, J. Cozic, and M. Gysel, 2008: The influence of small aerosol particles on the properties of water and ice clouds. *Faraday Discuss.*, **137**, 205–222.

Clark, T. L. and R. Farley, 1984: Severe downslope windstorm calculations in two and three spatial dimensions using anelastic interactive grid nesting: A possible mechanism for gustiness. *J. Atmos. Sci.*, **41**, 329–350.

Colle, B. A., 2004: Sensitivity of orographic precipitation to changing ambient conditions and terrain geometries: An idealized modeling perspective. *J. Atmos. Sci.*, **61**, 588–606.

Cozic, J., B. Verheggen, E. Weingartner, J. Crosier, K. Bower, M. Flynn, H. Coe, S. Henning, M. Steinbacher, M. C. Coen, A. Petzold, and U. Baltensperger, 2007: Chemical composition of free tropospheric aerosol for PM1 and coarse mode at the high alpine site Jungfraujoch. *Atmos. Chem. Phys. Dis.*, **7**, 12145–12184.

Davies, H., 1976: A lateral boundary formulation for multi-level prediction models. *Q. J. R. Meteorol. Soc.*, **102**, 405–418.

Doms, G. and U. Schättler, 2002: A description of the nonhydrostatic regional model LM. Part I: Dynamics and numerics. Technical report, Deutscher Wetterdienst, Offenbach, Germany.

Herzog, H.-J., G. Vogel, and U. Schubert, 2002: LLM - a nonhydrostatic model applied to high-resolving simulations of turbulent fluxes over heterogeneous terrain. *Theor. and Appl. Climatol.*, **73**, 67–86.

Jiang, Q. and R. Smith, 2003: Cloud timescales and orographic precipitation. *J. Atmos. Sci.*, **60**, 1543–1559.

Kirshbaum, D. J. and D. R. Durran, 2004: Factors governing cellular convection in orographic precipitation. *J. Atmos. Sci.*, **61**, 682–698.

— 2005: Observations and modeling of banded orographic convection. *J. Atmos. Sci.*, **62**, 1463–1479.

Muhlbauer, A. and U. Lohmann, 2008: Sensitivity studies of the role of aerosols in warm-phase orographic precipitation in different dynamical flow regimes. *J. Atmos. Sci.*, in press.

Roe, G. H. and M. Baker, 2006: Microphysical and geometrical controls on the pattern of orographic precipitation. *J. Atmos. Sci.*, **63**, 861–880.

Schär, C., D. Leuenberger, O. Fuhrer, D. Lüthi, and C. Girard, 2002: A new terrain-following vertical coordinate formulation for atmospheric prediction models. *Mon. Weather Rev.*, **130**, 2459–2480.

Seifert, A. and K. D. Beheng, 2006: A two-moment cloud microphysics parameterization for mixed-phase clouds. Part I: Model description. *Meteorol. Atmos. Phys.*, **92**, 45–66.

Smith, R., 1979: The influence of mountains on the atmosphere. *Adv. Geophys.*, **21**, 87–230.

Smith, R. and I. Barstad, 2004: A Linear Theory of Orographic Precipitation. *J. Atmos. Sci.*, **61**, 1377–1391.

Spichtinger, P., 2004: *Eisübersättigte Regionen*. Ph.D. thesis, Deutsches Zentrum für Luft- und Raumfahrt, 208 pp.

Steppeler, J., G. Doms, U. Schättler, H. Bitzer, A. Gassmann, U. Damrath, and G. Gregoric, 2003: Meso-gamma scale forecasts using the nonhydrostatic model LM. *Meteorol. Atmos. Phys.*, **82**, 75–96.

Weingartner, E., S. Nyeki, and U. Baltensperger, 1999: Seasonal and diurnal variation of aerosol size distributions ($10 < \mathrm{d} < 750$ nm) at a high-alpine site (Jungfraujoch 3580 m asl). *J. Geophys. Res.*, **104**, 26809–26820.

Wicker, L. J. and W. C. Skamarock, 2002: Time-splitting methods for elastic models using forward time schemes. *Mon. Weather Rev.*, **130**, 2088–2097.